Tribology International 211 (2025) 110868

Contents lists available at ScienceDirect

Tribology International

journal homepage: www.elsevier.com/locate/triboint

Rolling contact fatigue perspective of damage mechanism in 3D printed 17–4 PH stainless steel

Nicola Zani [a,*,1], Candida Petrogalli [a,2], Kang Shu [b,3], Francesco Cantaboni [a,4], Paola Serena Ginestra [a,5]

[a] Department of Mechanical and Industrial Engineering, University of Brescia, Via Branze, 38, Brescia 25123, Italy
[b] College of Mechanical Engineering, Hunan Institute of Science and Technology, Xueyuan Road, 439, Yueyang 414006, China

ARTICLE INFO

Keywords:
Rolling Contact Fatigue
17–4PH Stainless Steel
Crack Propagation
Laser Powder Bed Fusion

ABSTRACT

This work investigates the rolling contact fatigue (RCF) behaviour of as-built 17–4PH stainless steel produced by Laser Powder Bed Fusion (L-PBF). Cyclic twin-disc tests were performed under various lubrication (oil and water) and loading conditions (1400–2000 MPa) to replicate service-like stresses. Experimental results highlight the dominant role of lubrication in damage progression. Oil delays crack initiation and limits surface degradation, whereas water intensifies pitting and crack branching due to hydraulic pressurization. Fracture surfaces reveal fatigue-dominated mechanisms with limited influence from melt pool boundaries. Crack depth and morphology vary with contact stress and lubrication, showing that fluid entrapment significantly affects propagation. These findings support the development of tailored post-processing and lubrication strategies for enhancing the durability of AM components in rolling applications.

1. Introduction

Rolling Contact Fatigue (RCF) is a critical failure mode in mechanical components subjected to cyclic rolling loads, such as bearings, gears, and railway wheels. It manifests as surface or subsurface crack initiation and propagation, ultimately leading to material spalling and component failure. RCF is driven by repeated Hertzian contact stresses, which induce shear stress below the surface, where microstructural discontinuities such as inclusions, porosity, and phase transformations can act as stress concentrators. The damage mechanisms involved include plastic deformation, crack nucleation, and fatigue-induced material degradation, all of which contribute to reducing the operational life of rolling components. The two primary failure mechanisms in RCF are surface-initiated pitting and subsurface spalling [1,2]. Surface pitting is typically caused by asperities, lubrication deficiencies, and external debris, which create stress concentrations that facilitate crack formation. Conversely, subsurface spalling originates from cyclic shear stresses at the depth of maximum Hertzian stress, often exacerbated by material inhomogeneities. In traditional wrought materials, subsurface-initiated cracks tend to propagate along microstructural features such as grain boundaries and inclusions, while in additively manufactured (AM) materials, unique processing-induced characteristics like anisotropic solidification structures and residual stresses may influence fatigue performance [3]. Laser Powder Bed Fusion (L-PBF) 3D-printed metals usually exhibit reduced fatigue performance compared to their conventionally manufactured counterparts, primarily due to inherent defects such as internal porosity and surface roughness [4,5]. These defects can serve as initiation sites for fatigue cracks, significantly impacting the fatigue life of L-PBF components. Additionally, the anisotropic microstructures resulting from the layer-by-layer fabrication process can influence fatigue behaviour, necessitating optimized processing parameters and post-processing treatments to enhance fatigue resistance [6]. The fatigue properties of L-PBF metals significantly impact their performance in traditional fatigue tests, such as axial

* Corresponding author.
E-mail address: nicola.zani@unibs.it (N. Zani).
[1] ORCID ID: 0000–0001-6808–8852
[2] ORCID ID: 0000–0002-1774–3914
[3] ORCID ID: 0000–0002-0834–6423
[4] ORCID ID: 0000–0003-4208–2430
[5] ORCID ID: 0000–0002-3858–7789

https://doi.org/10.1016/j.triboint.2025.110868
Received 24 March 2025; Received in revised form 29 May 2025; Accepted 6 June 2025
Available online 11 June 2025
0301-679X/© 2025 The Author(s). Published by Elsevier Ltd. This is an open access article under the CC BY license (http://creativecommons.org/licenses/by/4.0/).

fatigue, rotating bending, and four-point bending tests [7]. In high-cycle fatigue tests, the defects act as stress concentrators, leading to premature failure, while in low-cycle fatigue, the anisotropic microstructure and strain localization can influence crack propagation behaviour [8]. RCF tests can be performed on LPBF samples to explore their behaviour under cyclic rolling loads, which are particularly relevant for applications in bearings, gears, and rail components. Moreover, RCF testing would provide more specific insights into the role of surface roughness, subsurface defects, and material anisotropy in rolling fatigue performance of 3D printed metals exploiting the potential applications of these components in industry. Recent studies confirm that anisotropy in AM microstructures strongly influences crack propagation under RCF conditions. For instance, Hassila et al. [9] demonstrated in Inconel 625 that build orientation and scan strategy significantly affect fatigue damage evolution, with cracks propagating differently depending on grain alignment and internal defects. Additionally, comparative studies on AM and wrought 316 L stainless steels [10] showed that SLM-fabricated components often exhibit higher wear resistance under dry sliding due to finer microstructures, though the presence of porosity remains a critical factor for crack nucleation under rolling loads. In gears produced via LPBF, Zhang et al. [11] observed that initial surface pitting preceded deeper material degradation, with the rougher surfaces and residual defects of AM parts accelerating fatigue-related wear compared to conventional counterparts. Moreover, tests on 17–4PH gears produced through bound metal deposition have highlighted that finer printing resolutions and post-machining steps significantly reduce noise, wear, and crack initiation, emphasizing the interplay between process parameters and RCF behaviour [12].

Subsurface-initiated fatigue occurs due to cyclic shear stresses in the Hertzian stress zone, where cracks propagate within the bulk material before reaching the surface. Donzella et al. [13] demonstrated that inclusions, such as sulfides, act as preferential sites for crack nucleation, with cracks growing parallel to the rolling surface before branching out. Rejith et al. [14] found that inclusion-rich steels like AISI 440 C have lower RCF resistance compared to cleaner, fine-carbide steels like Cronidur-30. Xia et al. [15] observed that when surface roughness is low, failure shifts from surface pitting to subsurface spalling, particularly in highly finished components subjected to cyclic loads. Additional damage mechanisms in RCF include plastic deformation, delamination, and material spalling. Accumulated plastic strain can lead to microstructural changes and crack nucleation, while fatigue cracks often propagate along melt pool boundaries in additively manufactured materials or carbide/matrix interfaces in steels. Rejith et al. [14] noted that in AISI 440 C, cracks frequently followed carbide segregation bands, accelerating delamination. Kurosaka et al. [16] studied Mode II shear-dominated crack propagation in railway wheels, showing that crack growth behaviour depends on defect orientation and stress conditions. Ultimately, rolling contact fatigue failure is a complex process influenced by surface integrity, microstructure, and stress distribution. A deeper understanding of these mechanisms is essential for optimizing material processing, selecting post-treatments, and improving the design of high-performance rolling components.

17–4 PH stainless steel is widely used in aerospace, automotive, and structural applications due to its high strength, corrosion resistance, and precipitation-hardening capability. However, its behaviour in L-PBF differs significantly from that of conventionally processed material [17,18]. Cecchel et al. [19] highlighted that L-PBF 17–4 PH, in the as-built condition, exhibits a highly anisotropic microstructure dominated by columnar δ-ferrite grains, retained austenite, and metastable martensite. The rapid solidification of L-PBF leads to the formation of a dendritic solidification structure, which is distinct from the fully martensitic microstructure found in wrought materials. This unique microstructural configuration modifies crack initiation and propagation paths, influencing fatigue resistance. The presence of retained austenite in as-built samples reduces mechanical strength, while the high cooling rates suppress equilibrium transformations, stabilizing δ-ferrite, which can act as preferential crack paths under cyclic loading.

In L-PBF-processed 17–4 PH, fatigue cracks typically initiate at surface defects or internal porosity. Bonaiti et al. [20] investigated bending fatigue in L-PBF-produced gears, demonstrating that crack nucleation frequently occurs at the surface due to high roughness and lack-of-fusion defects. The study revealed that cracks propagate along melt pool boundaries and columnar grain structures, following the anisotropic solidification pattern of the AM process. Unlike conventional 17–4 PH, where fatigue cracks propagate randomly through a more homogeneous martensitic matrix, in the as-built L-PBF condition, cracks tend to grow preferentially along weak interlayer regions, reducing fatigue resistance and accelerating failure.

To mitigate these effects, post-processing techniques such as Hot Isostatic Pressing (HIP), machining, and heat treatments are commonly employed. However, Concli et al. [21] observed that even after HIP, L-PBF 17–4 PH still exhibits lower fatigue resistance compared to wrought materials due to residual microstructural anisotropy. Furthermore, Cecchel et al. [19] noted that solution heat treatments improve mechanical properties by transforming δ-ferrite into a refined martensitic structure, but this transformation is often incomplete in thicker AM parts, leading to non-uniform mechanical performance across different geometries.

Similarly, Haghdadi et al. [22] examined Inconel 625 and identified that process-induced defects, such as lack-of-fusion porosity, caused subsurface crack formation and premature failure under cyclic contact loading. Arivu et al. [23] extended this analysis to L-PBF processed Inconel 718, demonstrating that heat treatment significantly improves fatigue life by restoring strengthening precipitates and homogenizing microstructure. These findings highlight that L-PBF-produced materials exhibit a general trend of lower fatigue resistance due to process-induced defects and microstructural anisotropy, which must be carefully controlled through optimized post-processing strategies. Hassila et al. [9] investigated the influence of build orientation and microstructural anisotropy on the RCF performance of L-PBF Inconel 625. Specimens with the cylinder axis parallel to the build direction (i.e., built vertically, with the rolling plane perpendicular to the build layers) exhibited gradual damage accumulation, characterized by multiple shallow cracks and a steady increase in vibration amplitude during testing. Conversely, cylinders with the axis perpendicular to the build direction (i.e., built horizontally, with the rolling plane aligned with the build layers) showed sudden localized failure, marked by fewer but deeper cracks and an abrupt rise in vibration levels. These behaviours were attributed to the columnar grain structure aligned along the build direction, which significantly affects crack initiation and propagation under cyclic rolling loads. The study highlights the key role of build orientation in controlling fatigue damage evolution and dynamic response in additively manufactured components subjected to RCF.

This study aims to investigate the rolling contact fatigue behaviour of as-built L-PBF 17–4 PH stainless steel, with a particular focus on the damage mechanisms that develop under cyclic loading conditions. Understanding the fatigue response of this material is crucial for its application in high-performance structural components subjected to repeated rolling contact stresses. The research explores the correlation between microstructural features, crack initiation and propagation mechanisms, and overall fatigue performance, providing a comprehensive assessment of the material's behaviour in its additively manufactured state. Through experimental testing and microstructural analysis, the findings offer valuable insights into the underlying mechanisms that govern damage evolution in rolling contact applications, contributing to the broader understanding of fatigue performance in additively manufactured stainless steels. This knowledge can serve as a basis for optimizing manufacturing parameters and material design to enhance the reliability and durability of components exposed to cyclic contact loads.

2. Materials and methods

The samples of 17–4PH stainless steel were fabricated using Laser Powder Bed Fusion (L-PBF) technology. ProX® DMP 100 printer (Laser Power: 100 W, © 2025 3D Systems, Inc., Wilsonville, Oregon, USA) was used for the production in a controlled nitrogen inert gas atmosphere (O_2 < 0.01 %). Fig. 1a-b shows the drawing of the specimens. The process parameters were previously optimized by the supplier [© 2025 3D Systems, Inc., Wilsonville, Oregon, USA] and previously applied [17, 24,25] to achieve the best reduction of internal defects and enhance the surface integrity results. The set of process parameters considered for the L- PBF experiments are used to calculate laser energy density using Eq. (1).

$$E_p = \frac{P}{h\,v\,t} \tag{1}$$

where, E_p is energy density (J/mm^3), P is laser power (W), v is scan speed (mm/s), t is layer thickness (mm), and h is hatch spacing (mm). The v was set at 300 mm/s, the h at 50 μm and t was kept at 30 μm. The powder used for these samples was the LaserForm 17–4PH (A) 17–4 PH gas-atomized powder. The batch properties are available online and in literature [26]. The chemical composition of LaserForm 17–4PH (A) corresponds to a stainless steel 17–4 PH alloy according to ASTM F899, A564, A693 and UNS S17400 specifications (Table 1). The samples were printed using 3D XPert software, (ProX® DMP 100, © 2025 3D Systems, Inc.) that allowed the positioning and the design of the support material as shown in Fig. 1c. The mechanical properties tested on parts manufactured with standard parameters on a ProX DMP printer are reported in Table 1.

The typical microstructure of 17–4 PH alloy produced by L-PBF is clearly visible. The presence of partially overlapped melt pools, formed due to the melting of metal powders under the laser action, is present and scan tracks identifying the path of the laser during the manufacturing process are clearly recognizable. Fig. 2 reports the microstructure with Kalling chemical etching on a rolling plane (plane parallel to the print) and the EDS analysis. Mosaic structure is typical of untreated additive and the presence of nitrogen-driven austenite due to the stabilised elements that allowed the formation of austenite, only partially transformed into martensite during rapid cooling. The hardness was measured at multiple points on a diametral plane and on the surface, yielding a value of 330 ± 4 HB.

The as-built condition of 17–4 PH stainless steel is predominantly composed by columnar δ-ferrite grains, while small islands of martensite are also observed, particularly along melt pool boundaries. Referring to Fig. 2, as already demonstrated by the authors with EDS results on as built 17–4 PH samples in [17], points 1 and 2 show chromium contents of 17 % and nickel of 4.5–4.7 %, while point 3 reveals a significantly higher copper concentration (>23 wt%). This is consistent with the formation of Cu-rich segregations or ε-Cu particles, frequently observed in the as-built conditions due to incomplete diffusion during solidification. The rapid solidification inherent to the LPBF process promotes high cooling rates (~10^6 K/s), which are sufficient to initiate martensite formation [19]. However, the formation is incomplete due to the presence of retained austenite and the influence of alloying elements like Ni and N, which stabilize the austenitic phase locally.

Cyclic contact tests were performed using a twin-disc testing rig [27–29]. The apparatus consists of two independently rotating discs that are pressed together under a predefined normal load, applied via a servo-hydraulic actuator. The rotational speed of the discs can be precisely adjusted to replicate different operating conditions, while sensors continuously monitor and record parameters such as normal force, torque, and rotational speed. For each test and lubrication condition, three replicate specimens were evaluated to assess the repeatability of the results.

The specimens were tested under three different load levels: 12 kN, 15.6 kN, and 24.5 kN, corresponding to nominal Hertzian contact pressures of 1400 MPa, 1600 MPa, and 2000 MPa, respectively. The counter-body disc was made of high-hardness tool steel, ensuring a greater hardness than the tested 17–4PH specimens. The tests were carried out in pure rolling conditions at a rotational speed of 750 rpm. To investigate the effect of contaminants on material response, two different lubricating conditions were considered: water mixed with glycol and oil with a flow rate of 6×10^{-3} m^3/s. The test was considered complete when surface spalling due to contact fatigue occurred. Since determining the exact number of cycles to failure is complex, an alternative approach was adopted using accelerometer data mounted on the machine's spindles. As reported in previous studies conducted with this test bench, accelerometer data provide an effective indicator of surface damage progression. After an initial set of trial tests, a stopping criterion was established: the test was interrupted when the accelerometer associated with the additive-manufactured specimen reached a threshold value of 0.7 m/s^2. The friction coefficient was estimated by dividing the torque couple measured with the torque meter of the test bench by the specimen radius and the normal contact load. The contact surface was acquired by a 2D/3D profile sensor Wenglor MLWL171, which allows determining the surface roughness R_a by the laser triangulation method Subsequently, small pieces with pits were cut from the specimens to analyze the damage of surface, longitudinal section and transverse section, as shown in Fig. 4.

The surface damage were directly analyzed using an ultra-depth of field 3D microscopic system (KEYENCE VHX-5000, Japan) and scanning electron microscope (SEM, Phenom Pro-SE, Netherlands). The small pieces for analyzing longitudinal section and transverse section were embedded in resin, then ground by SiC abrasive paper with different mesh numbers and finally polished by diamond powders with size of 2.5 μm. Similarly, the subsurface damage of longitudinal section and transverse section were also analyzed using the ultra-depth of field 3D microscopic system. The samples were chemically etched using Kalling reagent, prepared with 5 g of $CuCl_2$, 100 ml of ethanol, and 100 ml of

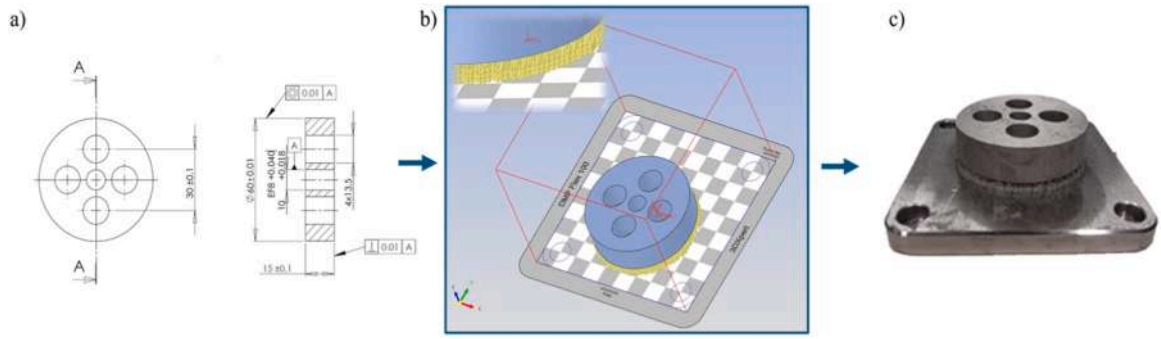

Fig. 1. (a) Technical drawing of the specimens; (b) Printer software visualization showing the support structures between the build plate and the specimen; (c) Specimen manufactured using L-PBF technology on a support structure.

Table 1
Chemical composition of LaserForm® 17–4PH (A), UNS S17400 and mechanical properties of as-built 17–4PH (1Tested on ASTM E8M specimens with circular cross sections type 4; 2Tested with Charpy V-notch impact test specimens type A at room temperature).

Element	Cr	Ni	Cu	Nb + Ta	Si, Mn	C	P, S	Fe
Weight [%]	15.00 – 17.50	3.00 – 5.00	3.00 – 5.00	0.15 – 0.45	< 1.00	< 0.07	< 0.04	Balance
Mechanical Property	Young Modulus [GPa]	Ultimate Strength [MPa]	Yield Strength [MPa]	Elongation at Break (%)	Hardness, Rockwell C	Impact Toughness [J]	Relative Density	
Standard	ASTM E8M	ASTM E8M	ASTM E8M	ASTM E8M	ASTM E18	ASTM E23	(pixel-based)	
Value	190 ± 17	1100 ± 90	830 ± 110	19 ± 4	32 ± 4	71 ± 20	> 99.9 %	

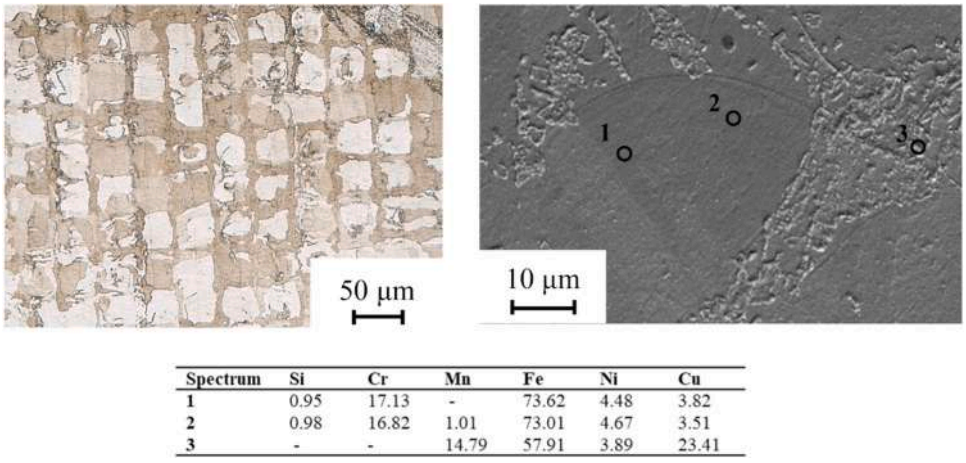

Spectrum	Si	Cr	Mn	Fe	Ni	Cu
1	0.95	17.13	-	73.62	4.48	3.82
2	0.98	16.82	1.01	73.01	4.67	3.51
3	-	-	14.79	57.91	3.89	23.41

Fig. 2. Optical micrograph and SEM images of 17–4PH as-built microstructure and chemical elements measured by EDS (in weight%).

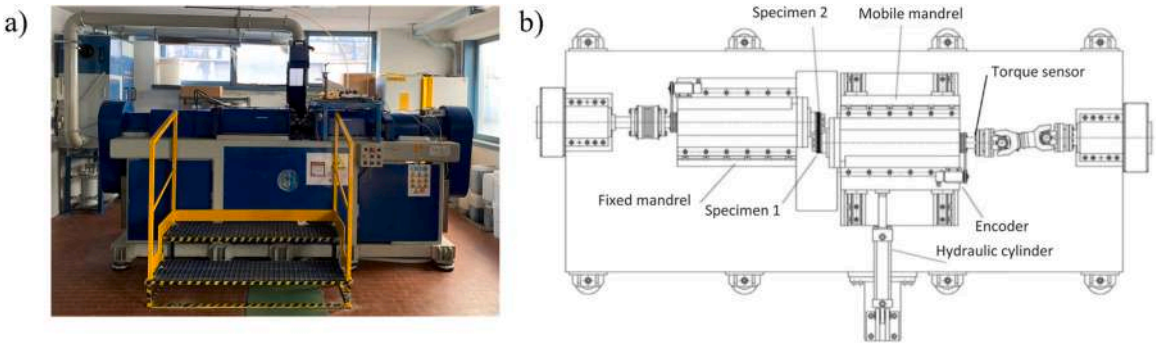

Fig. 3. a) Bidisc test bench; b) Technical diagram of the bench showing the main components.

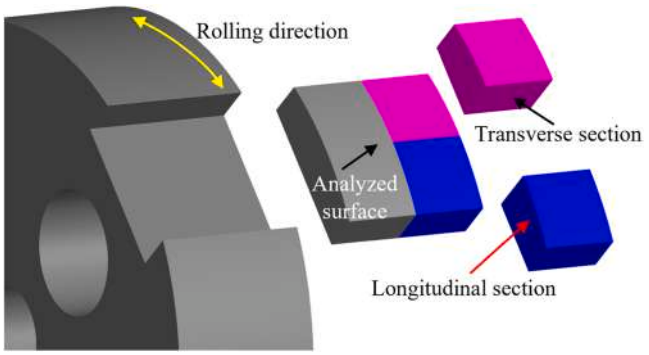

Fig. 4. Microanalysis position details of specimens after tests.

HCl, to reveal the microstructural features of the material. Additionally, the crack dimensions (crack-tip-opening angle, crack depth, crack length) were measured and counted using the measurement software of the ultra-depth of field 3D microscopic system, as shown in Fig. 5.

3. Results

The Wöhler diagram (Fig. 6) illustrates the relationship between applied pressure and fatigue life (the average value of the three repeated tests is reported with the scatter band).

Specimens tested with oil exhibited a longer fatigue life than those tested with water, highlighting the beneficial effect of oil in mitigating rolling contact fatigue (RCF) damage.

The friction coefficient trends are illustrated in Fig. 7. Regardless of the contaminant used, the friction behaviour follows a characteristic transient phase: after an initial peak, the coefficient gradually decreases until stabilizing. For tests conducted with oil, the steady-state friction coefficient stabilizes around 0.027, whereas for tests performed with

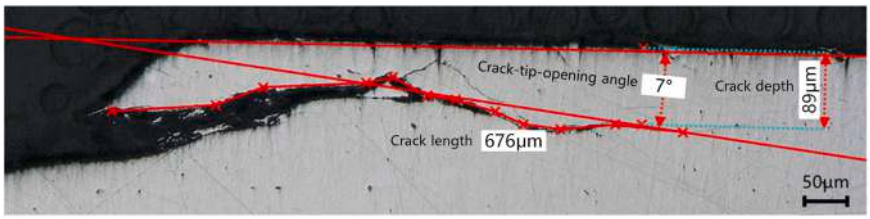

Fig. 5. Measurement method of crack dimensions.

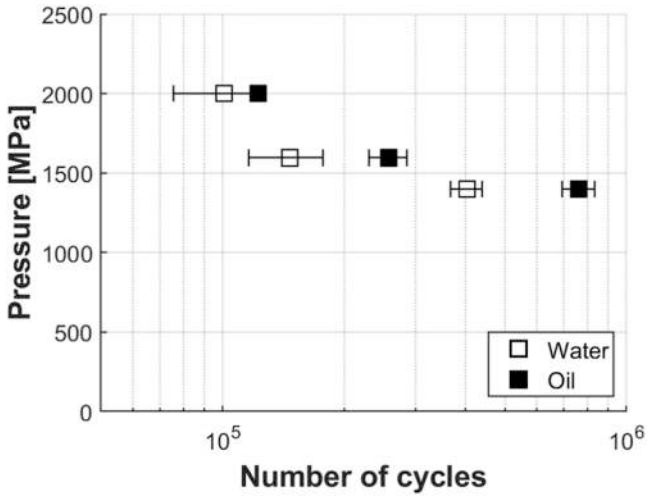

Fig. 6. Pressure life diagram for specimens subjected to RCF tests.

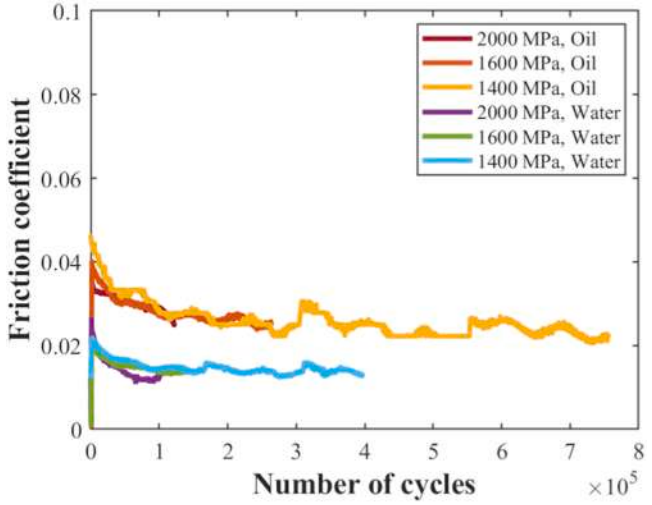

Fig. 7. Trend of the friction coefficients in the tests.

water, it reaches a lower equilibrium value of approximately 0.013. This difference suggests that water lubrication leads to a significantly lower friction regime, potentially influencing the fatigue behaviour of the tested materials. The periodic variations observed in the friction coefficient under the 1400 MPa load with oil lubrication, as shown in Fig. 7, can likely be attributed to the combined effects of surface evolution and third-body interactions. At this intermediate load level, micro-pitting or mild surface wear may intermittently modify the contact topography, influencing the friction response over time. Additionally, the formation and detachment of wear debris or oxide particles can act as a third body within the contact, momentarily altering the local friction conditions before being expelled or integrated into the surface. These phenomena can lead to the recurring fluctuations observed during the test cycles.

The analysis of spalling severity at the end of the test reveals distinct differences depending on the applied contact pressure and the lubricant used (Fig. 8). At 2000 MPa, the water-lubricated sample exhibits localized but deep spalling, indicating significant contact fatigue, whereas the oil-lubricated sample shows less extensive but still well-defined damage, suggesting a slightly improved protective effect. At 1600 MPa, the water-lubricated surface presents a concentrated and deep fracture zone, while the oil-lubricated surface displays more fragmented spalling, possibly indicating a mitigating effect of the lubricant. At 1400 MPa, the most severe damage is observed in the water-lubricated condition, with a widespread and highly rough fracture surface. In contrast, the oil-lubricated sample exhibits more diffused but shallower damage, reinforcing the protective role of the lubricant. The presence of surface pitting across several tested conditions further supports these trends. Pits, particularly prominent in water-lubricated specimens, are typically associated with early-stage rolling contact fatigue (RCF) and serve as precursors to crack initiation and eventual spalling. Similar phenomena have been reported in the literature. Liu et al. [30] observed that untreated surfaces in SEBM-manufactured (Selective Electron Beam Melting) are prone to pit formation due to high surface roughness and insufficient hardness—factors that accelerate fatigue degradation. Zhou et al. [10] found that 316 L stainless steel produced via MEAM (Metal Extrusion Additive Manufacturing) exhibited increased pitting in dry conditions, while fluid-mediated environments helped reduce surface wear through debris entrapment mechanisms. In our study, the evolution and morphology of pitting under different pressures and lubricants provide a meaningful indication of fatigue progression. The correlation between pit development and crack initiation observed here aligns with these earlier findings and reinforces the critical influence of lubrication and surface integrity in delaying RCF damage in AM components.

Fig. 9 provides a quantitative analysis of surface roughness and the spatial distribution of the R_a parameter along the circumference of the tested specimens, highlighting the influence of contact pressure and lubricant used.

The average roughness R_a graph clearly shows that water-lubricated samples experience a more significant increase in roughness compared to oil-lubricated ones. This aligns with the observations from the second image, where surface damage appears more extensive and deeper in water-lubricated conditions. This suggests that water, unlike oil, provides less protection against contact fatigue, contributing to higher residual roughness after testing. The analysis of roughness distribution along the angular position indicates that, at higher pressures (1600 and 2000 MPa), the damage is characterized by localized roughness peaks, especially in water-lubricated conditions, confirming more pronounced spalling formation. Conversely, in oil-lubricated tests, roughness remains lower and more uniform, indicating better lubricating performance in reducing wear and the propagation of surface fractures. To further analyze the surface degradation mechanisms, the roughness of the contact surfaces was also evaluated separately in areas outside the pitting and spalling zones. This analysis revealed that, in the undamaged regions, the roughness remained substantially lower, with R_a values around 13±0.7 µm for oil-lubricated and water-lubricated ones (slightly lower than the average R_a of not tested samples, that is 19±3 µm). This

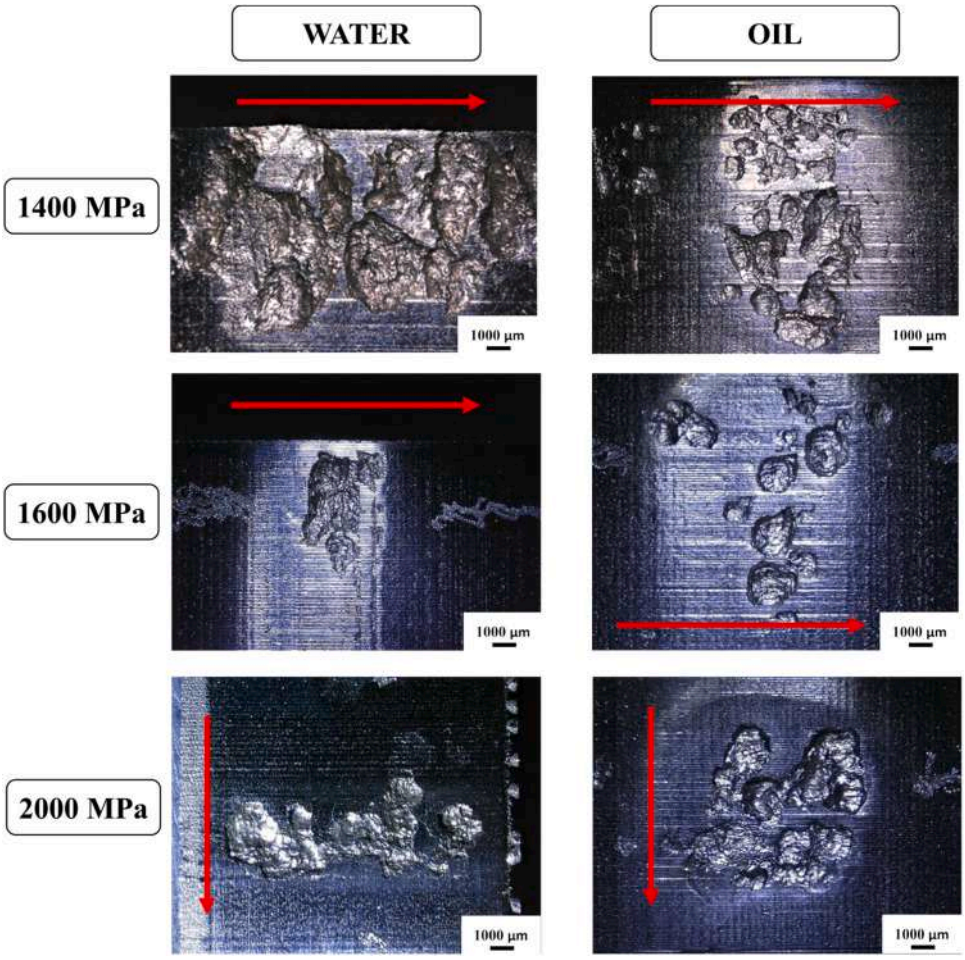

Fig. 8. Pit morphology under different loading and contaminant conditions (the arrows denote the rolling direction).

reduction in roughness can be attributed to the localized plastic deformation and micro-smoothing effects occurring during the initial loading cycles, which promote the flattening of asperities and a better conformity between the contacting surfaces, even in the absence of significant wear. Similar trends have been reported in the literature for additively manufactured components subjected to cyclic loading. Zhou et al. [10] observed that 316 L stainless steel fabricated via MEAM exhibits increased roughness and wear severity under dry conditions, while fluid-based environments can offer partial mitigation through debris entrapment. In a comparative study, Farij et al. [31] showed that lubricating conditions significantly influence tribological response in AM Inconel 718, with advanced lubrication strategies leading to substantial reductions in both wear and surface roughness. The present results are consistent with these findings, showing that oil lubrication contributes to a more stable and uniform surface finish compared to water, which under high pressure conditions promotes localized material degradation. The angular variation in roughness observed in water-lubricated samples also supports the idea that low-viscosity fluids are less effective at maintaining surface integrity under RCF, resulting in more severe roughness peaks and heterogeneous damage patterns.

The microstructural analysis provides key insights into wear mechanisms and rolling contact fatigue damage under cyclic loading. Surface and cross-sectional examinations reveal substantial differences in crack initiation and propagation, influenced by lubrication type and contact stress levels.

The damage mechanisms observed in the tested specimens reflect typical rolling contact fatigue failure phenomena, with significant differences depending on the lubrication condition. Surface pitting (Fig. 10a), commonly associated with early-stage RCF damage in bearing steels, was evident in several samples. The measured pit depths ranged between 80 and 100 µm, indicating initial fatigue degradation. These pits, if not monitored, can evolve into crack initiation sites, leading to crack propagation (Fig. 10b) and, eventually, spalling [32,33]. The presence of pitting is particularly relevant in high-stress applications, as the interaction between surface asperities and cyclic loading accelerates fatigue crack nucleation. The obtained micrographic images clearly reveal that the cracks do not preferentially propagate along the melt pool boundaries or solidification lines; instead, they cut across the microstructure, suggesting that the dominant fracture mechanisms are governed by local stress concentrations and cyclic loading effects, rather than being constrained or guided by the anisotropic features introduced during the additive manufacturing process. This observation aligns with the findings of Concli et al. [21], who similarly reported that in L-PBF 17–4 PH steel, fatigue cracks predominantly follow stress-driven paths independent of the solidification structure.

A detailed crack propagation analysis highlights the presence of branched cracks (Fig. 11), particularly in water-lubricated samples. The branching behaviour aligns with the observations found in the literature [34,35], that described a similar mechanism in rolling contact fatigue failures under fluid-lubricated conditions. In these samples, crack bifurcation is attributed to fluid entrapment within the crack cavities. As the rolling load cycles continue, the trapped fluid experiences pressure variations, exerting additional forces on the crack faces and promoting crack growth [13,36–41]. This hydraulic pressurization mechanism accelerates both crack opening and bifurcation, increasing the

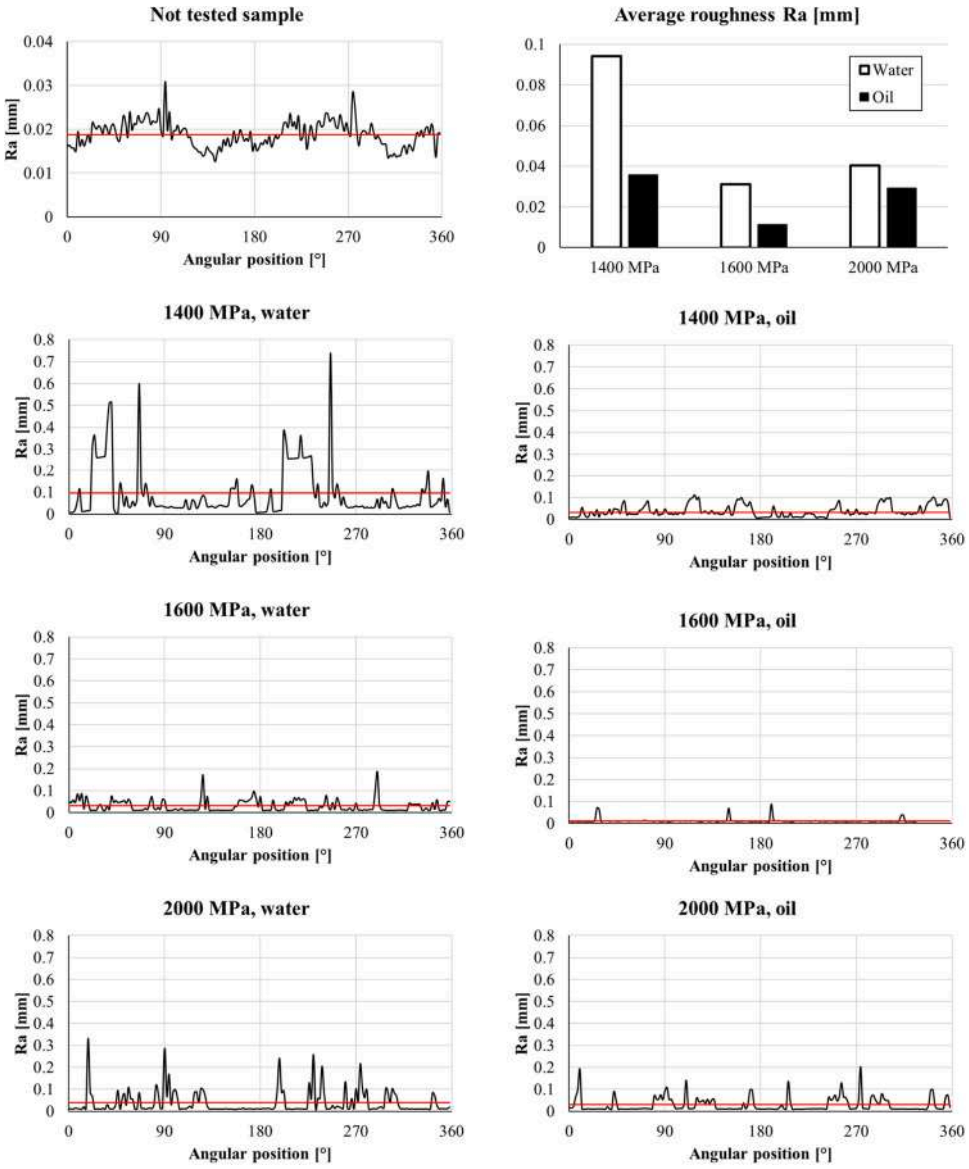

Fig. 9. Surface roughness analysis before and after testing at different pressures and lubrication conditions.

likelihood of shelling. In agreement with the stage-based models proposed by Rycerz et al. [40], the cracks initially propagate at shallow angles relative to the surface (typically 20–30°) under shear dominated stress fields. In later stages, a transition to parallel propagation occurs, influenced by hertzian stresses and fluid-pressure effects. This is consistent with the observed evolution from oblique initiation to interconnected crack networks in water-lubricated specimens. The shelling phenomenon, observed in the transverse section of the most severely damaged samples, is characterized by deep interconnected cracks leading to material detachment.

In addition to crack branching, the micrographs reveal the presence of debris particles within the crack cavities (Fig. 12). Literature suggests that these particles can influence crack propagation in two contrasting ways. In some cases, debris may accumulate within the crack, acting as a barrier that impedes further crack growth by preventing crack tip opening; in other instances, the debris may alter the local contact pressure distribution, creating stress concentration points that accelerate crack propagation [40,42–47]. The influence of debris on crack evolution is highly dependent on its composition and morphology, which should be further analyzed to assess its role in the observed failure mechanisms.

In Fig. 13, the unpolished cross-sections along the rolling plane reveal distinct damage morphologies under varying load and lubrication conditions; Fig. 14 shows the same sections but with a higher magnification (except for the specimen tested with oil at 1600 MPa). At the highest load, crater-like defects are evident, with coplanar cracks initiating from their lower extremities. This suggests that excessive loading has promoted pit-induced damage rather than rolling contact fatigue. The presence of these pits implies that local material removal has occurred before significant crack propagation, a phenomenon often associated with severe stress concentrations and lubrication breakdown. The coexistence of pitting and coplanar cracks is consistent with observations by Donzella et al. [13,48] and Rejith et al. [14], who showed that surface defects under high contact stresses promote subsequent subsurface fracture and eventual spalling. This mechanism supports the observed damage patterns where initial surface degradation triggers more complex crack networks. Furthermore, such damage morphology aligns with the findings of Xia et al. [15], who highlighted that high surface roughness under heavy loads can significantly reduce RCF life by fostering early pit formation and crack nucleation near the surface. These mechanisms are especially severe when lubricant film thickness is insufficient, which exacerbates asperity contact and stress localization.

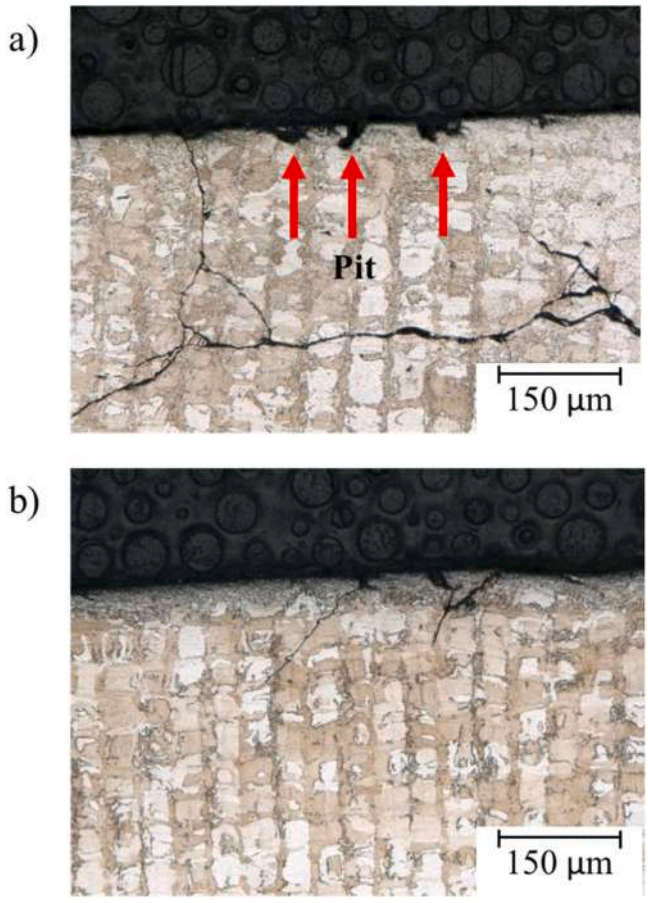

Fig. 10. a) Surface pit detail (1600 MPa, water); b) surface crack initiating from pit (1600 MPa, oil) (rolling direction from left to right).

At 1600 MPa, the lubrication medium plays a crucial role in crack development. Under water lubrication, extensive branched cracks are visible, indicating a more aggressive damage evolution. Conversely, under oil lubrication, no significant cracks are detected at the same magnification, suggesting that the oil film effectively mitigates direct asperity contact and reduces the severity of surface damage, likely delaying crack nucleation.

At lower loads, crack branching occurs in both lubrication conditions, with no clear suppression effect from oil. This suggests that at reduced stress levels, the fatigue mechanism dominates over pit-induced damage, and lubricant type alone is insufficient to prevent crack initiation. Similar trends have been reported in studies on rolling-sliding wear, where subsurface stress thresholds dictate the transition from plastic deformation to fatigue crack nucleation, regardless of lubricant viscosity. These results confirm that at lower stress levels, crack initiation is governed by shear accumulation and slip band formation, as also suggested by theoretical models in Olver [49] and Rycerz et al. [40]. While lubricant type may influence the rate of propagation, it does not fully prevent initiation once local stresses exceed the fatigue limit. The observed crack morphology at lower loads further supports the hypothesis that lubricant effectiveness is load-dependent, with higher stresses amplifying the distinction between water- and oil-lubricated conditions.

At higher magnification (Fig. 15), the damage mechanisms under different lubrication conditions become clearer. Under water lubrication, the absence of an effective protective film leads to the early nucleation of cracks, which are wider and highly branched. Numerous secondary cracks (branch cracks) originate from the main fracture path, and significant debris accumulation is observed within the cracks. These debris particles, often oxidized, act as local stress concentrators, further promoting crack deflection and unstable propagation. This phenomenon is consistent with observations of fatigue striations and multi-layer cracks formation reported by Yan et al. [50]. Conversely, with oil lubrication, the cracks are cleaner and narrower, with fewer branches and minimal evidence of particle entrapment. The fracture surfaces appear smoother, indicating a delayed crack propagation and a more stable fatigue behaviour. This can be attributed to the oil film effectively separating the contact surfaces, reducing direct asperity contact and the severity of localized plastic deformation. Even at higher loads (2000 MPa), the oil-lubricated specimens show a limited development of complex crack networks, and the presence of large spalling craters is less frequent compared to water-lubricated conditions. These findings underscore the importance of lubrication regime, surface condition, and load in determining the dominant RCF mechanism. As highlighted by both Donzella et al. [13] and Xia et al. [15], the transition between surface-initiated and subsurface-initiated fatigue is load- and lubrication-dependent, and the presence of inclusions, roughness features, or even oxide particles can determine the fatigue life trajectory. The coexistence of pitting, crack networks, and spalling in our specimens reflects this complex interplay, further confirming the need to tailor surface preparation and lubrication strategy to the expected operating load regime.

Observations from rolling plane reveals the presence of subsurface cracks as well, which develop beneath the contact surface due to cyclic shear stress. These cracks, commonly found in RCF failures, often originate from non-metallic inclusions or microstructural heterogeneities where stress concentration is high [13,48,51–54]. However, subsurface cracks are significantly more limited compared to surface cracks, which appear to be the dominant failure mode in the tested specimens.

Wear patterns confirm a strong dependence on lubricant viscosity and its ability to maintain film stability under rolling contact. Water, with lower viscosity, infiltrates cracks more effectively, exacerbating propagation through pressurization effects. In contrast, oil, particularly in thickened grease formulations, enhances surface protection by forming a barrier that limits crack expansion and material loss.

The comparison between experimental crack depths and the

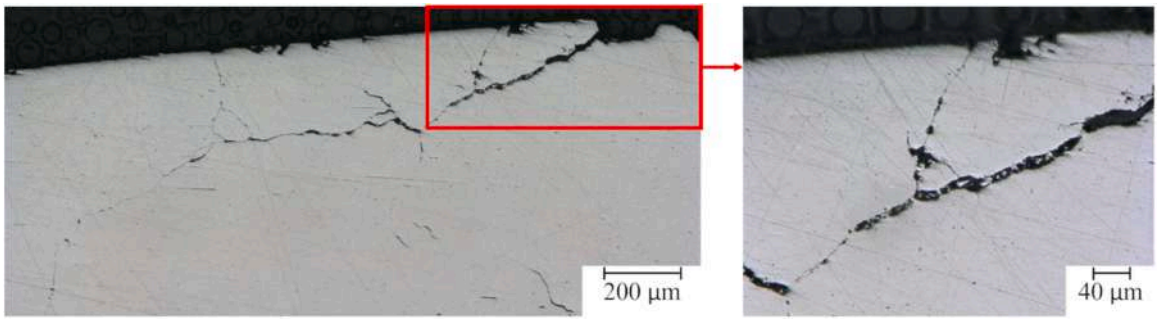

Fig. 11. Rolling contact fatigue branched crack and detail of shelling damage (1600 MPa, water) (rolling direction from left to right).

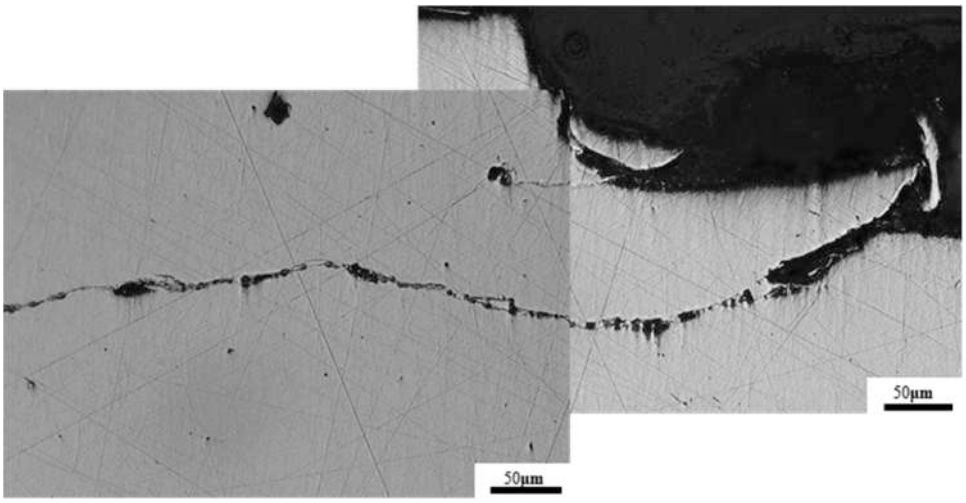

Fig. 12. Surface crack morphology with debris (2000 MPa, oil).

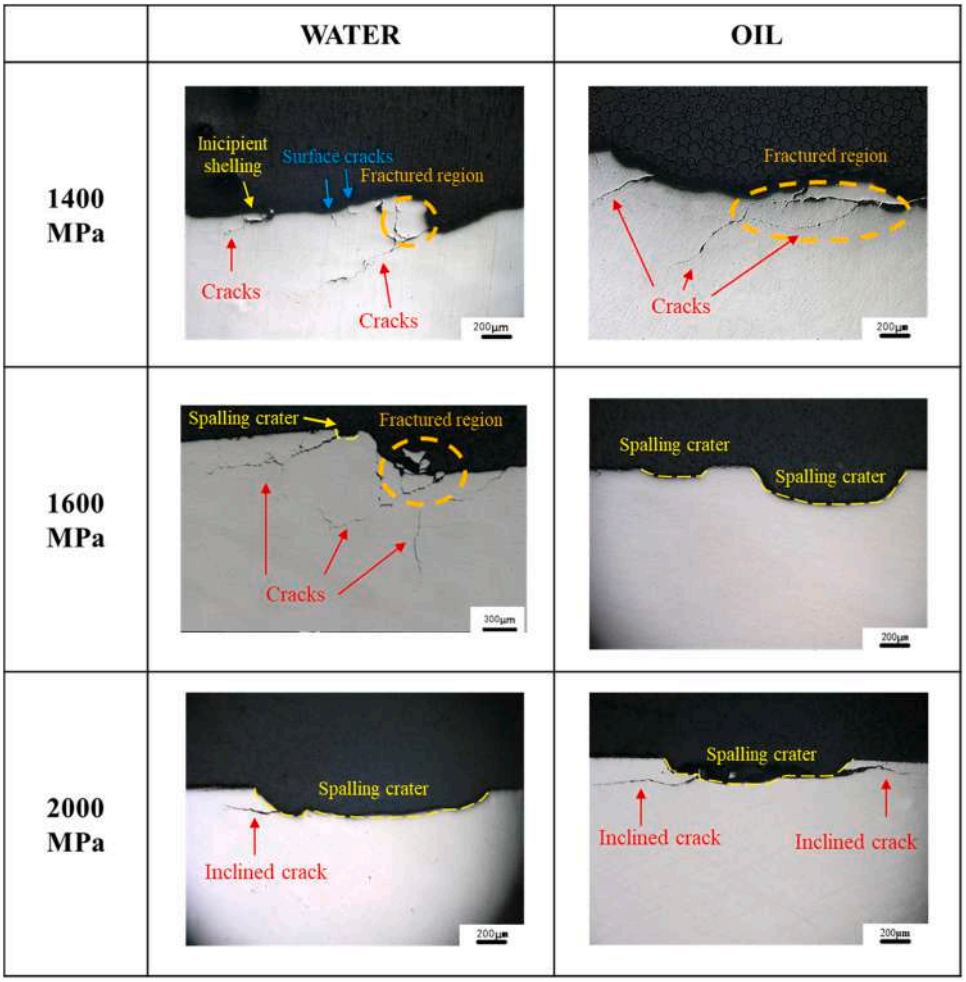

Fig. 13. Crack morphology under different contact pressure and contaminants (rolling direction from left to right).

theoretical depths of maximum subsurface shear stress according to Hertzian theory provides insights into crack propagation mechanisms. Theoretical models predict that, for a contact pressure of 2000 MPa, 1600 MPa, and 1400 MPa, the maximum subsurface shear stress occurs at depths of 286 μm, 326 μm, and 410 μm, respectively. However, experimental results indicate significantly greater crack depths, suggesting that additional factors, such as fluid penetration and microstructural influences, contribute to the observed deviation from Hertzian predictions. In the water-lubricated specimens, crack depths ranged from a minimum of 30 μm to a maximum of 237 μm, whereas in oil-lubricated samples, the minimum depth was 144 μm, and the maximum reached 309 μm. In the specimens tested at 1600 MPa with oil

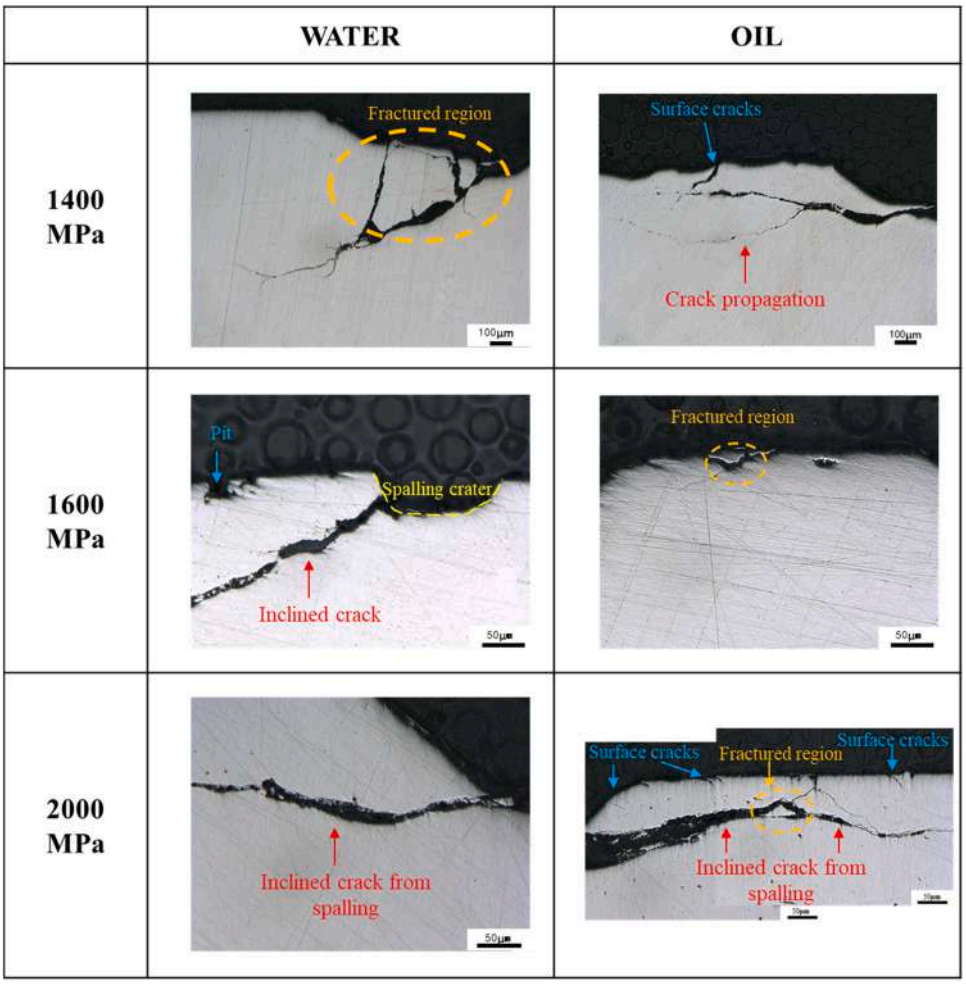

Fig. 14. Crack morphology under different contact pressure and contaminants (same cracks as Fig. 13, different magnification) (rolling direction from left to right).

lubrication, no evident rolling contact fatigue cracks were found, while in water-lubricated samples, numerous cracks with variable depths, ranging from 240 μm to a maximum of 866 μm, were observed. Notably, tested with water at 1600 MPa, exhibited the deepest cracks, indicating significant material degradation beyond the Hertzian estimate (Fig. 16). These results reinforce the hypothesis that fluid pressurization within cracks facilitates their growth beyond conventional limits. While oil lubrication effectively limited crack penetration depth, it was associated with greater crack lengths. In oil-lubricated samples, the maximum crack length reached 881μm, compared to 402 μm in water-lubricated conditions. This behaviour is consistent with the role of oil in reducing friction and stabilizing the lubricant film, thereby decreasing surface fatigue but allowing for more extensive lateral crack propagation.

Analysis of crack propagation in sections orthogonal to the rolling direction (Fig. 17) reveals distinct failure modes depending on the lubrication conditions. In water-lubricated samples, cracks tend to develop as deep, branched networks, often extending significantly into the material. This behaviour suggests that pressurized fluid infiltration within cracks plays a dominant role in crack growth. The hydraulic effect leads to crack opening and bifurcation, facilitating subsurface crack expansion and promoting material detachment through shelling mechanisms. The presence of interconnected cracks, as observed in several micrographs, confirms that fluid-assisted propagation is a major contributor to fatigue damage under water lubrication. Conversely, in oil-lubricated samples, longitudinal crack propagation appears more confined, with cracks generally remaining within the near-surface region. Despite spanning a considerable portion of the sample thickness, these cracks exhibit limited branching and reduced depth compared to water-lubricated specimens. This suggests that the presence of an oil film plays a protective role by reducing friction and stabilizing contact conditions, thereby limiting vertical crack penetration. However, oil lubrication appears to facilitate lateral crack extension, as cracks tend to propagate more along the rolling plane rather than into the depth of the material.

4. Conclusions

This study investigated the rolling contact fatigue (RCF) behaviour of 17–4PH stainless steel produced by Laser Powder Bed Fusion (L-PBF), with a focus on the effects of contact pressure and lubrication. Cyclic twin-disc tests were performed under both oil and water lubrication at different load levels, and damage mechanisms were assessed through surface and cross-sectional analyses. Although the specimens were manufactured using a single set of L-PBF parameters and tested with a single oil type, the results offer useful insights into the fatigue response of the material under controlled conditions. Key findings are summarized below:

- Lubrication type strongly influences fatigue response: oil delays crack initiation and reduces surface damage, while water promotes earlier pitting and more severe crack branching due to fluid pressurization.
- Surface roughness increases significantly under water lubrication, with more localized wear, whereas oil results in more uniform and lower roughness after testing.

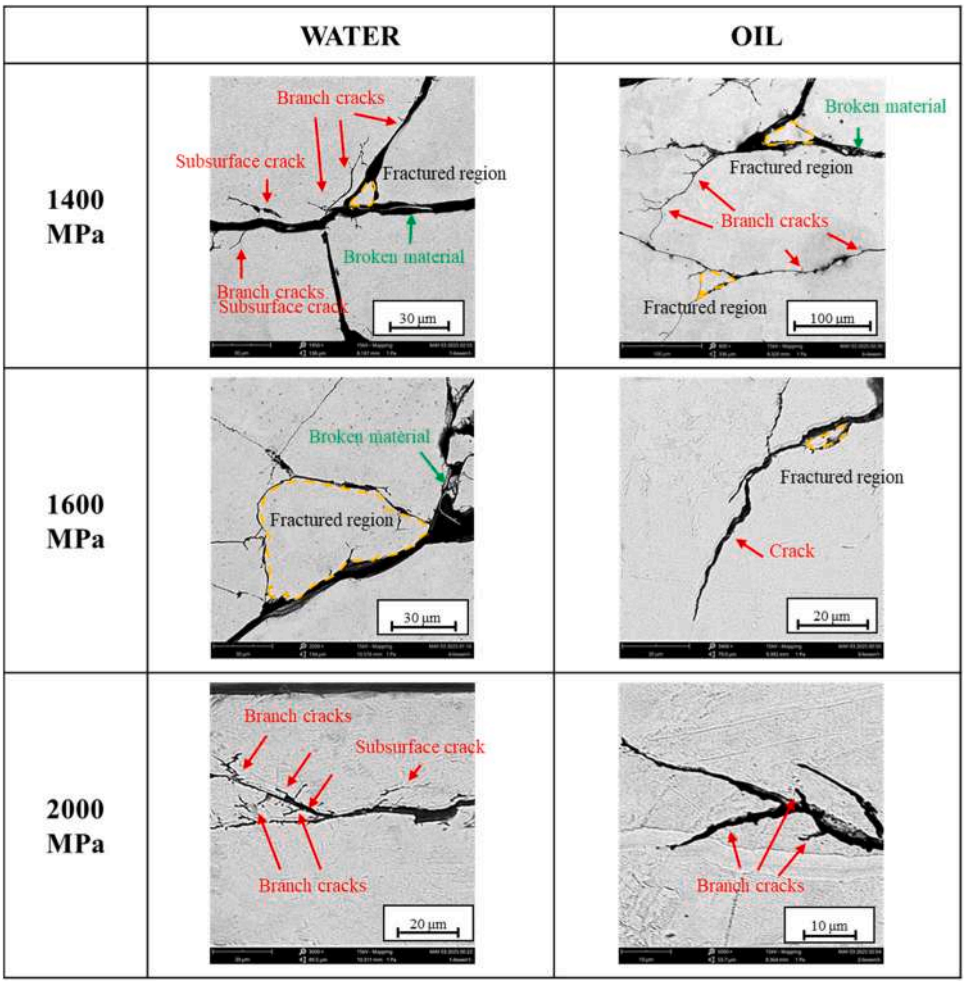

Fig. 15. Crack morphology under different contact pressure and contaminants (same cracks as Fig. 13, different magnification) (rolling direction from left to right).

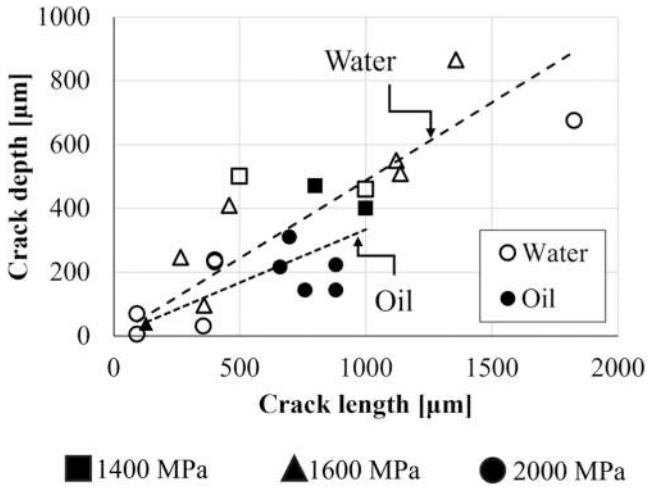

Fig. 16. Statistical distribution of cracks according to lubricant and contact pressure.

- Damage morphologies differ with testing conditions: water leads to deeper, branched, and interconnected cracks, often associated with shelling, while oil favours more lateral and confined crack propagation.
- Cracks propagate independently of melt pool boundaries, suggesting that local stress concentrations are the dominant driving force rather than microstructural orientation.
- Crack depth and length statistics confirm lubrication effects: water-lubricated samples show deeper cracks often exceeding Hertzian predictions, while oil-lubricated samples exhibit longer but shallower cracks.

While the present study does not allow for broad generalizations regarding the optimization of AM parameters or lubricant selection, the observed damage mechanisms provide a solid basis for future investigations. Future developments will include additional load levels to refine fatigue maps, direct comparison with conventionally manufactured (wrought) 17–4PH steels, and the evaluation of post-processing treatments such as heat treatment and Hot Isostatic Pressing to enhance fatigue resistance. These steps aim to support the design of more reliable AM components for rolling contact applications. Considering the promising results obtained under controlled lubrication conditions, potential applications of L-PBF 17–4PH stainless steel include critical mechanical components subjected to cyclic rolling loads, such as bearings, gears and rolling elements in power transmission systems. With appropriate post-processing and lubrication strategies, this material can also be considered for aerospace and automotive applications, where weight reduction, complex geometries, and high mechanical performance under dynamic loading are essential.

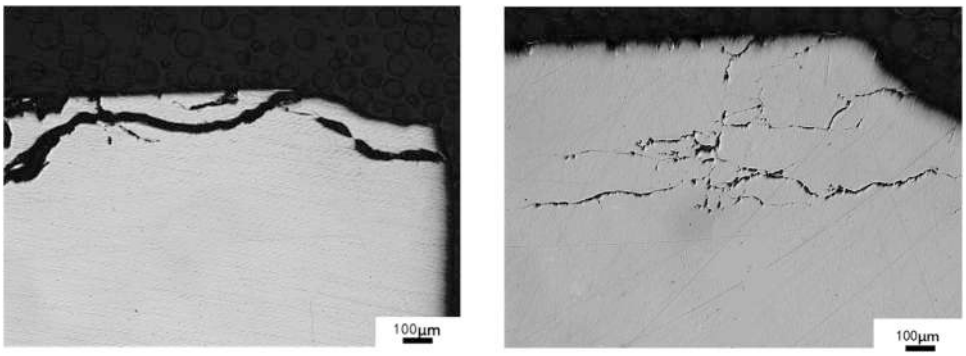

Fig. 17. Cross-sectional morphology of cracks on the transverse plane of samples tested at 1400 MPa (oil on the left, water on the right).

CRediT authorship contribution statement

Kang Shu: Writing – review & editing, Validation, Methodology, Investigation. **Paola Serena Ginestra:** Writing – review & editing, Visualization, Resources, Methodology, Investigation, Conceptualization. **Francesco Cantaboni:** Writing – review & editing, Methodology, Investigation. **Candida Petrogalli:** Writing – review & editing, Resources, Methodology, Investigation, Data curation, Conceptualization. **Nicola Zani:** Writing – review & editing, Writing – original draft, Supervision, Resources, Methodology, Investigation, Data curation, Conceptualization.

Declaration of Competing Interest

The authors declare that they have no known competing financial interests or personal relationships that could have appeared to influence the work reported in this paper.

Data availability

Data will be made available on request.

References

[1] Sadeghi F, Jalalahmadi B, Slack TS, Raje N, Arakere NK. A review of rolling contact fatigue. J Tribol 2009;131:1–15. https://doi.org/10.1115/1.3209132/471354.
[2] Ekberg A, Åkesson B, Kabo E. Wheel/rail rolling contact fatigue - probe, predict, prevent. Wear 2014;314:2–12. https://doi.org/10.1016/j.wear.2013.12.004.
[3] Cantaboni F, Ginestra PS, Tocci M, Avanzini A, Ceretti E, Pola A. Compressive behavior of Co-Cr-Mo radially graded porous structures under as-built and heat-treated conditions. Fract Struct Integr 2022;16:490–504. https://doi.org/10.3221/IGF-ESIS.62.33.
[4] Li Z, Affolter C. High-Cycle fatigue performance of laser powder bed fusion Ti-6Al-4V alloy with inherent internal defects: a critical literature review. Met 2024;14:972. https://doi.org/10.3390/MET14090972.
[5] Sanaei N, Fatemi A. Analysis of the effect of surface roughness on fatigue performance of powder bed fusion additive manufactured metals. Theor Appl Fract Mech 2020;108:102638. https://doi.org/10.1016/J.TAFMEC.2020.102638.
[6] Oliveira JP, LaLonde AD, Ma J. Processing parameters in laser powder bed fusion metal additive manufacturing. Mater Des 2020;193:108762. https://doi.org/10.1016/J.MATDES.2020.108762.
[7] Santos L, de Jesus J, Borrego L, Ferreira JAM, Fernandes RF, da Costa JDM, et al. Fatigue behavior of hybrid components containing maraging steel parts produced by laser powder bed fusion. Met 2021;11:835. https://doi.org/10.3390/MET11050835.
[8] Sotelo L.D., Fuller A.J., Pratt C.S., Madireddy G., Karunakaran R., Sealy M.P., et al. Fatigue Performance of Bearing Rollers Manufactured by Laser Powder Bed Fusion. ASTM Spec Tech Publ 2024;STP 1649:227–48. https://doi.org/10.1520/STP164920220115.
[9] Hassila CJ, Harlin P, Wiklund U. Rolling contact fatigue crack propagation relative to anisotropies in additive manufactured inconel 625. Wear 2019;426–427:1837–45. https://doi.org/10.1016/J.WEAR.2019.01.085.
[10] Zhou S, Yang Y, Zhu J, Wanyan S, Su K, Ma F, et al. Tribological behavior of 316L stainless steel fabricated using metal extrusion additive manufacturing under dry and simulated body Fluid-Lubricated conditions. Adv Eng Mater 2024;26:2400294. https://doi.org/10.1002/ADEM.202400294.
[11] Zhang Y, Daman AAA, He P, Li X, Borghesani P, Peng Z. Wear study of additively manufactured 316L stainless steel gears. Wear 2025:205796. https://doi.org/10.1016/J.WEAR.2025.205796.
[12] Basak AK, Ghasseb J, Pramanik A. Performance of gears manufactured through additive manufacturing. Met 2025;15. https://doi.org/10.3390/met15010063.
[13] Donzella G, Faccoli M, Mazzù A, Petrogalli C, Desimone H. Influence of inclusion content on rolling contact fatigue in a gear steel: experimental analysis and predictive modelling. Eng Fract Mech 2011;78:2761–74. https://doi.org/10.1016/j.engfracmech.2011.07.011.
[14] Rejith R, Arivu Y, Kesavan D, Chakravarthy P, Narayana Murty SVS. Relating rolling contact fatigue (RCF) life to the microstructure evolution in aerospace grade bearing steels: a comparison of Cronidur-30 with AISI 440C. Int J Fatigue 2024;186:108421. https://doi.org/10.1016/J.IJFATIGUE.2024.108421.
[15] Xia Z, Wu D, Zhang X, Wang J, Han EH. Rolling contact fatigue failure mechanism of bearing steel on different surface roughness levels under heavy load. Int J Fatigue 2024;179:108042. https://doi.org/10.1016/J.IJFATIGUE.2023.108042.
[16] KUROSAKA R., KATO T., MAKINO T. 鉄道車輪鋼を対象とした破壊力学的手法による転動疲労条件下のモードIIき裂進展速度評価法. 日本機械学会論文集 2024;90:24–00010. https://doi.org/10.1299/TRANSJSME.24-00010.
[17] Cantaboni F, Tocci M, Ginestra PS, Pola A, Ceretti E. Production and characterization of lattice samples with solid shell in 17-4 PH stainless steel by laser powder bed fusion technology. Procedia Struct Integr 2024;53:65–73. https://doi.org/10.1016/J.PROSTR.2024.01.009.
[18] Abeni A, Ginestra PS, Attanasio A. Micro-milling of selective laser melted stainless steel. Lect Notes Mech Eng 2021:1–12. https://doi.org/10.1007/978-3-030-57729-2_1.
[19] Cecchel S, Ferraresi R, Magni M, Guerini L, Cornacchia G. Evolution of prototyping in automotive engineering: a comprehensive study on the reliability of additive manufacturing for advanced powertrain components. Frat Ed Integrita Strutt 2024;18:109–26. https://doi.org/10.3221/IGF-ESIS.68.07.
[20] Bonaiti L, Concli F, Gorla C, Rosa F. Bending fatigue behaviour of 17-4 PH gears produced via selective laser melting. Procedia Struct Integr 2019;24:764–74. https://doi.org/10.1016/j.prostr.2020.02.068.
[21] Concli F, Fraccaroli L, Nalli F, Cortese L. High and low-cycle-fatigue properties of 17–4 PH manufactured via selective laser melting in as-built, machined and hipped conditions. Prog Addit Manuf 2022;7:99–109. https://doi.org/10.1007/s40964-021-00217-y.
[22] Haghdadi N, Laleh M, Moyle M, Primig S. Additive manufacturing of steels: a review of achievements and challenges. J Mater Sci 2021;56:64–107. https://doi.org/10.1007/s10853-020-05109-0.
[23] Arivu Y, Ranju MR, Abhinand C, Padmapreetha R, Kesavan D. Contact fatigue studies on L-PBF processed IN718 alloy tested under no slip condition. Int J Fatigue 2023;173:107702. https://doi.org/10.1016/J.IJFATIGUE.2023.107702.
[24] Ginestra P.S., Riva L., Allegri G., Giorleo L., Attanasio A., Ceretti E. Analysis of 3D printed 17-4 PH stainless steel lattice structures with radially oriented cells. Ind 40 - Shap Futur Digit World - Proc 2nd Int Conf Sustain Smart Manuf S2M 2019 2019:136–41. https://doi.org/10.1201/9780367823085-25.
[25] Zapico P, Giganto S, Martínez-Pellitero S, Fernández-Abia AI, Castro-Sastre MÁ. Influence of laser energy in the surface quality of parts manufactured by selective laser melting. Ann DAAAM Proc Int DAAAM Symp, 29; 2018. p. 0279–86. https://doi.org/10.2507/29th.daaam.proceedings.040.
[26] https://www.3dsystems.com/materials/laserform-17–4ph. (accessed on 28 May 2025)
[27] Zani N, Petrogalli C. Predictive maps for the rolling contact fatigue and wear interaction in railway wheel steels. Wear 2022;510–511:204513. https://doi.org/10.1016/j.wear.2022.204513.
[28] Zani N, Mazzù A, Solazzi L, Petrogalli C. Examining wear mechanisms in railway wheel steels: experimental insights and predictive mapping. Lubricants 2024;12. https://doi.org/10.3390/lubricants12030093.
[29] Zani N, Petrogalli C, Battini D. Optimizing railway tribology: a systematic review and predictive modeling of Twin-Disc testing parameters. Lubricants 2024;12. https://doi.org/10.3390/lubricants12110382.
[30] Liu Z, Liu X, Liu R, Xiao Z, Sanderson J. Improved rolling contact fatigue performance of selective electron beam melted Ti6Al4V with the as-built surface using induction-heating assisted ultrasonic surface rolling process. Appl Surf Sci 2023;617:155467. https://doi.org/10.1016/j.apsusc.2022.155467.

[31] Saoud FAMBen, Korkmaz ME. Improvement in tribological properties of additively manufactured IN718 using low temperature lubricated environments. J Mater Eng Perform 2025. https://doi.org/10.1007/s11665-025-10818-1.
[32] Huang W, Cao X, Wen Z, Wang W, Liu Q, Zhu M, et al. A subscale experimental investigation on the influence of sanding on adhesion and rolling contact fatigue of Wheel/Rail under water condition. J Tribol 2017;139:1–8. https://doi.org/10.1115/1.4033100.
[33] Rejith R, Kesavan D, Chakravarthy P, Narayana Murty SVS. Bearings for aerospace applications. Tribol Int 2023;181:108312. https://doi.org/10.1016/j.triboint.2023.108312.
[34] Makino T, Kato T, Hirakawa K. The effect of slip ratio on the rolling contact fatigue property of railway wheel steel. Int J Fatigue 2012;36:68–79. https://doi.org/10.1016/j.ijfatigue.2011.08.014.
[35] Mazzù A, Provezza L, Zani N, Petrogalli C, Ghidini A, Faccoli M. Effect of shoe braking on wear and fatigue damage of various railway wheel steels for high speed applications. Wear 2019:434–5. https://doi.org/10.1016/j.wear.2019.203005.
[36] Ancellotti S, Benedetti M, Dallago M, Fontanari V. Fluid pressurization and entrapment effects on the SIFs of cracks produced under lubricated Rolling-Sliding contact fatigue. Procedia Struct Integr 2016;2:3098–108. https://doi.org/10.1016/J.PROSTR.2016.06.387.
[37] Donzella G, Faccoli M, Mazzù A, Petrogalli C, Roberti R. Progressive damage assessment in the near-surface layer of railway wheel-rail couple under cyclic contact. Wear 2011;271:408–16. https://doi.org/10.1016/j.wear.2010.10.042.
[38] Bodini I, Zani N, Petrogalli C, Mazzù A, Kato T, Makino T. Damage assessment in a wheel steel under alternated dry-lubricated contact by an innovative vision system. Wear 2023;530:205064. https://doi.org/10.1016/j.wear.2023.205064.
[39] Kunzelmann B, Rycerz P, Xu Y, Arakere NK, Kadiric A. Prediction of rolling contact fatigue crack propagation in bearing steels using experimental crack growth data and linear elastic fracture mechanics. Int J Fatigue 2023;168:107449. https://doi.org/10.1016/J.IJFATIGUE.2022.107449.
[40] Rycerz P, Olver A, Kadiric A. Propagation of surface initiated rolling contact fatigue cracks in bearing steel. Int J Fatigue 2017;97:29–38. https://doi.org/10.1016/J.IJFATIGUE.2016.12.004.
[41] Zaid M, Doquet V, Chiaruttini V, Depouhon P, Bonnand V, Pacou D. On the influence of secondary branches on crack propagation in rolling contact fatigue. Int J Fatigue 2024;182:108211. https://doi.org/10.1016/J.IJFATIGUE.2024.108211.
[42] Madia M, Vojtek T, Duarte L, Zerbst U, Pokorný P, Jambor M, et al. Determination of fatigue crack propagation thresholds for steel in presence of environmental effects. Int J Fatigue 2021;153:106449. https://doi.org/10.1016/J.IJFATIGUE.2021.106449.
[43] Duarte L, Schönherr JA, Madia M, Zerbst U, Geilen MB, Klein M, et al. Recent developments in the determination of fatigue crack propagation thresholds. Int J Fatigue 2022;164. https://doi.org/10.1016/j.ijfatigue.2022.107131.
[44] Maierhofer J, Simunek D, Gänser HP, Pippan R. Oxide induced crack closure in the near threshold regime: the effect of oxide debris release. Int J Fatigue 2018;117:21–6. https://doi.org/10.1016/J.IJFATIGUE.2018.07.021.
[45] Cvetkovski K, Ahlström J, Norell M, Persson C. Analysis of wear debris in rolling contact fatigue cracks of pearlitic railway wheels. Wear 2014;314:51–6. https://doi.org/10.1016/J.WEAR.2013.11.049.
[46] He CG, Huang YB, Ma L, Guo J, Wang WJ, Liu QY, et al. Experimental investigation on the effect of tangential force on wear and rolling contact fatigue behaviors of wheel material. Tribol Int 2015;92:307–16. https://doi.org/10.1016/j.triboint.2015.07.012.
[47] Wang C, Shi LB, Ding HH, Wang WJ, Galas R, Guo J, et al. Adhesion and damage characteristics of wheel/rail using different mineral particles as adhesion enhancers. Wear 2021;477:203796. https://doi.org/10.1016/J.WEAR.2021.203796.
[48] Donzella G, Mazzù A, Petrogalli C. Competition between wear and rolling contact fatigue at the wheel-rail interface: some experimental evidence on rail steel. Proc Inst Mech Eng Part F J Rail Rapid Transit 2009;223:31–44. https://doi.org/10.1243/09544097JRRT161.
[49] Olver AV. The mechanism of rolling contact fatigue: an update. Proc Inst Mech Eng Part J J Eng Tribol 2005;219:313–30. https://doi.org/10.1243/135065005X9808.
[50] Yan H, Wei P, Su L, Liu H, Wei D, Zhang X, et al. Rolling-sliding contact fatigue failure and associated evolutions of microstructure, crystallographic orientation and residual stress of AISI 9310 gear steel. Int J Fatigue 2023;170:107511. https://doi.org/10.1016/J.IJFATIGUE.2023.107511.
[51] Beretta S., Donzella G., Roberti R., Ghidini A. Contact fatigue propagation of deep defects in railway wheels. Fuentes M, Elices M, Martin-Meizoso A Martinez-Esnaola JM Proc 13th Eur Conf Fract – ECF13 San Sebastian, Spain, Oxford Elsevier 6–9 Sept 2000 n.d.:147–154.
[52] Wang WJ, Jiang WJ, Wang HY, Liu QY, Zhu MH, Jin XS. Experimental study on the wear and damage behavior of different wheel/rail materials. Proc Inst Mech Eng Part F J Rail Rapid Transit 2016;230:3–14. https://doi.org/10.1177/0954409714524566.
[53] José López-Uruñuela F, Fernández-Díaz B, Pinedo B, Aguirrebeitia J. Early stages of subsurface crack and WEC formation in 100Cr6 bearing steel under RCF and hydrogen influence. Int J Fatigue 2022;155:106587. https://doi.org/10.1016/J.IJFATIGUE.2021.106587.
[54] Ren Z, Li B, Zhou Q. Rolling contact fatigue crack propagation on contact surface and subsurface in mixed mode I+II+III fracture. Wear 2022;506–507:204459. https://doi.org/10.1016/J.WEAR.2022.204459.